

# Quantitative measurement of active dopant density distribution in phosphorus-implanted monocrystalline silicon solar cell using scanning nonlinear dielectric microscopy

K. Hirose,<sup>1</sup> K. Tanahashi,<sup>2</sup> H. Takato,<sup>2</sup> and Y. Cho<sup>1,a)</sup>

<sup>1</sup>Research Institute of Electrical Communication, Tohoku University, 2-1-1 Katahira, Aoba-ku, Sendai 980-8577, Japan

<sup>2</sup>Fukushima Renewable Energy Institute, National Institute of Advanced Industrial Science and Technology, Koriyama, Fukushima 963-0298, Japan

(Received 22 March 2017; accepted 7 July 2017; published online 17 July 2017)

The performance of silicon (Si) solar cells is dependent on the active dopant distribution in emitters. Estimation of the dopant distribution in a Si solar cell fabricated by ion implantation is difficult due to the pyramidal surface texture of the emitter. Here, we investigate the active dopant distribution in a P-implanted Si solar cell using scanning nonlinear dielectric microscopy (SNDM). SNDM and  $dC/dz$ -SNDM are complementarily applied to visualize the carrier distribution in the cross section of the Si solar cell. The carrier density in the emitter is calibrated using the SNDM data obtained from Si standard samples. The results show that the dopant distribution can be described as the sum of two Gaussian functions distributed over the vertical direction of the pyramidal faces. The three-dimensional (3D) dopant distribution is estimated from the superposition of the P distributions at each pyramidal face. The estimated 3D dopant distribution is in good agreement with the SNDM measurement results. *Published by AIP Publishing.*

[<http://dx.doi.org/10.1063/1.4994813>]

Crystalline silicon (Si) solar cells have occupied an important place in the solar cell market and have been researched to achieve further reduction in costs and improvement in the conversion efficiency. Ion implantation has been proposed as a technique for achieving low-cost and high-efficiency solar cells because of the high degree of freedom it provides for designing devices.<sup>1,2</sup> A typical Si solar cell has a pyramidal texture at the surface to improve light absorption.<sup>3</sup> The dopant is implanted into each of the textured faces at different angles. An annealing process is subsequently performed to recover the crystallinity of the implanted surface region and for the diffusion of the implanted dopant. However, estimating the dopant distribution in ion implanted Si solar cells is difficult due to the complex three-dimensional (3D) textured structure of the solar cell. The conversion efficiency of an ion-implanted solar cell is influenced by the ion implantation and annealing parameters. Therefore, evaluation of the dopant distribution is very important in order to realize highly efficient solar cells. Scanning capacitance microscopy (SCM)<sup>4</sup> has already been applied to qualitatively observe the dopant distribution in the emitter of a solar cell,<sup>5</sup> whereby the active dopant in a phosphorus (P)-diffused emitter and in a P-implanted emitter of a solar cell was visualized. However, the density of the active dopant has not been quantitatively determined.

In this letter, we report the active dopant density distribution in a P-implanted Si solar cell determined using scanning nonlinear dielectric microscopy (SNDM).<sup>6</sup> SNDM is a scanning probe microscopy technique that has much higher capacitance sensitivity ( $10^{-22}$  F) than SCM. SNDM and  $dC/dz$ -SNDM,

which is an extended SNDM mode, are complementarily applied to evaluate the P-implanted Si solar cell.

An SNDM probe, which consists of a conductive cantilever tip attached to a gigahertz (GHz)-range free-running LC (inductor-capacitor) oscillator, is used for both SNDM and  $dC/dz$ -SNDM measurements. The oscillating frequency deviation of the SNDM probe is proportional to the variation of the tip-sample capacitance,  $C_s$ . In SNDM,  $C_s$  is modulated by a sinusoidal voltage from the sample stage. Therefore, the SNDM signal is proportional to  $dC_s/dV$ . The polarity of  $dC_s/dV$  corresponds to the carrier polarity, and the magnitude of  $dC_s/dV$  reflects the carrier density. However, the carrier density distribution cannot be determined from  $dC_s/dV$  alone, due to the contrast reversal phenomenon.<sup>7</sup> The magnitude of  $dC_s/dV$  becomes largest at a certain carrier density and becomes close to zero as the carrier density becomes higher or lower with respect to that density. The  $dC_s/dV$  data combined with  $dC/dz$ -SNDM were used to determine the carrier density distribution. For  $dC/dz$ -SNDM,  $C_s$  is modulated by the tip-sample distance,  $z$ . The  $dC/dz$ -SNDM signal is proportional to  $dC_s/dz$ , which reflects the carrier density rather than the carrier polarity. The sign of  $dC_s/dz$  is always negative because  $C_s$  decreases as the tip leaves the sample surface. The magnitude of the  $dC_s/dz$  signal reflects the capacitance when the tip is in contact with the surface. Therefore, the magnitude of the  $dC/dz$ -SNDM signal corresponds to the absolute value of the carrier density without contrast reversal. Thus, the  $dC/dz$ -SNDM signal can be used to avoid misjudgment caused by the two value function problem with the contrast reversal phenomenon of the  $dC_s/dV$  measurement.

P was implanted into the textured surface with an acceleration energy of 10 keV, a tilt angle of 35°, and a step angle

<sup>a)</sup>E-mail: yasuocho@riec.tohoku.ac.jp

of  $15^\circ$ . Annealing was conducted at  $900^\circ\text{C}$  for 10 min. The implantation dose was  $4 \times 10^{15} \text{ cm}^{-2}$ . Silicon nitride (SiN) with the thickness of 80 nm was then deposited on the textured surface as a passivation layer. The P-implanted Si solar cell was cross-sectioned almost parallel to the (110) face of the Si, i.e., parallel to an edge of the squared base of the pyramidal texture. The cross section of the solar cell was finished by chemomechanical polishing. The cross section was measured using SNDM with contact mode atomic force microscopy (AFM), and dC/dz-SNDM was performed using tapping mode AFM.

Figures 1(a) and 1(b) show the respective SNDM and dC/dz-SNDM images obtained. The dashed line indicates the SiN/Si interface determined from the sample topography. Two pyramidal structures can be seen in the images. The bright region and the dark region in Fig. 1(a) represent n- and p-type semiconductors, respectively. The bright region in Fig. 1(b) contains a high carrier density. Figure 2 shows line profiles measured along the arrows in Fig. 1. The horizontal axis is the distance from the SiN/Si interface. Figure 2(a) shows that the SNDM signal has a peak at the center of the n-type region due to the contrast reversal phenomenon. In contrast, the dC/dz-SNDM signal decreases from the textured surface to the bulk, as shown in Fig. 2(b), which corresponds to a decreasing electron density.

Both p-type and n-type Si staircase standard samples were prepared for calibration of the carrier density. The samples had 7 layers and 6 layers, respectively, each with a different carrier density. The carrier density of each layer was obtained from secondary ion mass spectroscopy (SIMS) measurements and ranged from  $1 \times 10^{16}$  to  $1 \times 10^{20} \text{ cm}^{-3}$ . The Si standard samples were polished at the same time as the Si solar cell. Therefore, it was assumed that the P-implanted Si solar cell and the standard sample have the same surface conditions. The standard samples were measured after the SNDM measurement of the P-implanted Si solar cell. The detailed SNDM data obtained from those staircase standard samples are shown in Fig. 3 with the dopant profile data by Secondary Ion Mass Spectrometry (SIMS). If the dopant type (n- and p-) or semiconductor material are different, the experimental dC/dV signal strength from the sample with the same carrier

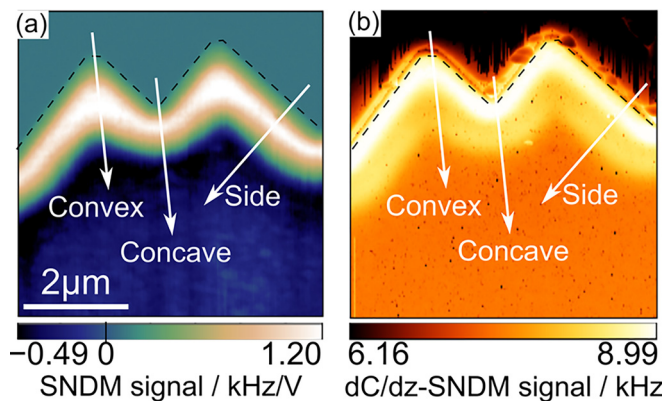


FIG. 1. (a) SNDM and (b) dC/dz-SNDM images of the cross section of a P-implanted Si solar cell. Dashed lines indicate the SiN/Si interface determined from the topography. The polarity of the SNDM signal corresponds to the carrier polarity. The magnitude of the dC/dz-SNDM signal corresponds to the carrier density.

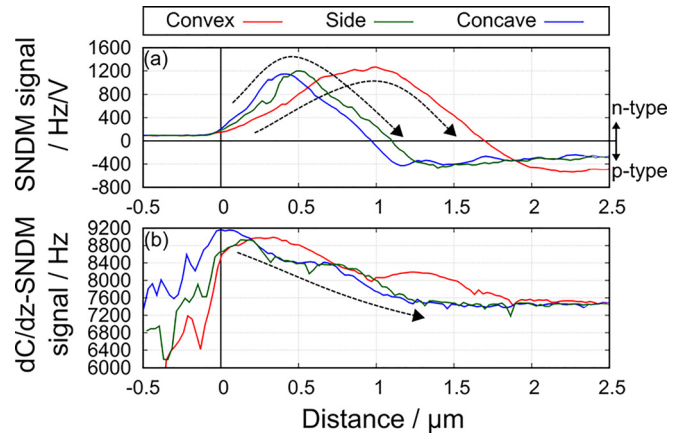


FIG. 2. Line profiles of (a) SNDM and (b) dC/dz-SNDM signals measured along the dashed line in Fig. 1. The SNDM signal reverses contrast at the center of the n-type region. The dC/dz-SNDM signal decreases from the textured surface to the bulk.

concentrations is different. Therefore, in this study, we measured both p-type and n-type Si standard samples. Figure 4(a) shows SNDM results calibrated by the SIMS dopant concentration data for the standard samples. The magnitude of the SNDM signal changes with the carrier density. A calibration curve was calculated using an empirical fitting function on the basis of the least squares method. Figure 4(b) shows the two-dimensional carrier density distribution converted from the data of SNDM image [Fig. 1(a)] using the calibration curve. Line profiles obtained from the data shown in Fig. 4(b) are shown in Fig. 4(c). The electron density decreases exponentially from the surface to the bulk. The hole density in the p-type bulk region is about  $1 \times 10^{15} \text{ cm}^{-3}$ , which is of the same order as the hole density calculated from the substrate resistivity. In the depletion layer,  $C_s$  is influenced by both the p- and n-type layers. Therefore, the calibrated results below about  $1 \times 10^{15} \text{ cm}^{-3}$  in Figs. 4(b) and 4(c) may not be correct.

The active dopant in the side position is one-dimensionally distributed along the direction of the arrow, as shown in Fig. 4(b). Therefore, the P distribution in the side region was analyzed on the basis of the implanted P distribution in the flat (not textured) substrate. The distribution can be roughly described as two distinct regions, i.e., the surface and tail regions.<sup>8</sup> Point defects and dopant ions form pairs and diffuse together.<sup>9</sup> In the surface region, the point defect density is lower than the impurity density, whereas the point defect density is comparable with the dopant density in the tail region. A Gaussian function was applied to the P distribution at the surface and tail regions. The two dashed lines in Fig. 4(c) show the fitting results. The function was fitted in the range of over  $1 \times 10^{16} \text{ cm}^{-3}$  because the carrier density was not equal to the P density in the depletion region. A joined half Gaussian function,<sup>10</sup> which includes the reflection effect at the surface, was used for fitting in the surface region. As shown in Fig. 4(c), two Gaussian functions describe the P distribution well. The dose calculated from the integral of the fitting curve was about  $7 \times 10^{15} \text{ cm}^{-2}$ , which was of the same order as the actual implantation dose. The error from the correct value stems from the fact that we made rough assumption

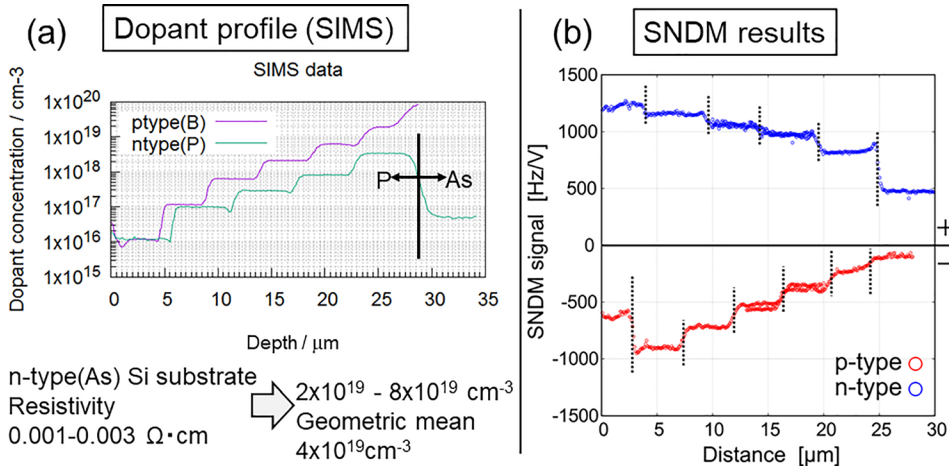


FIG. 3. (a) Dopant profiles of p-type and n-type Si staircase standard samples measured by Secondary Ion Mass Spectrometry (SIMS). (b) Corresponding SNDM results for two standard samples.

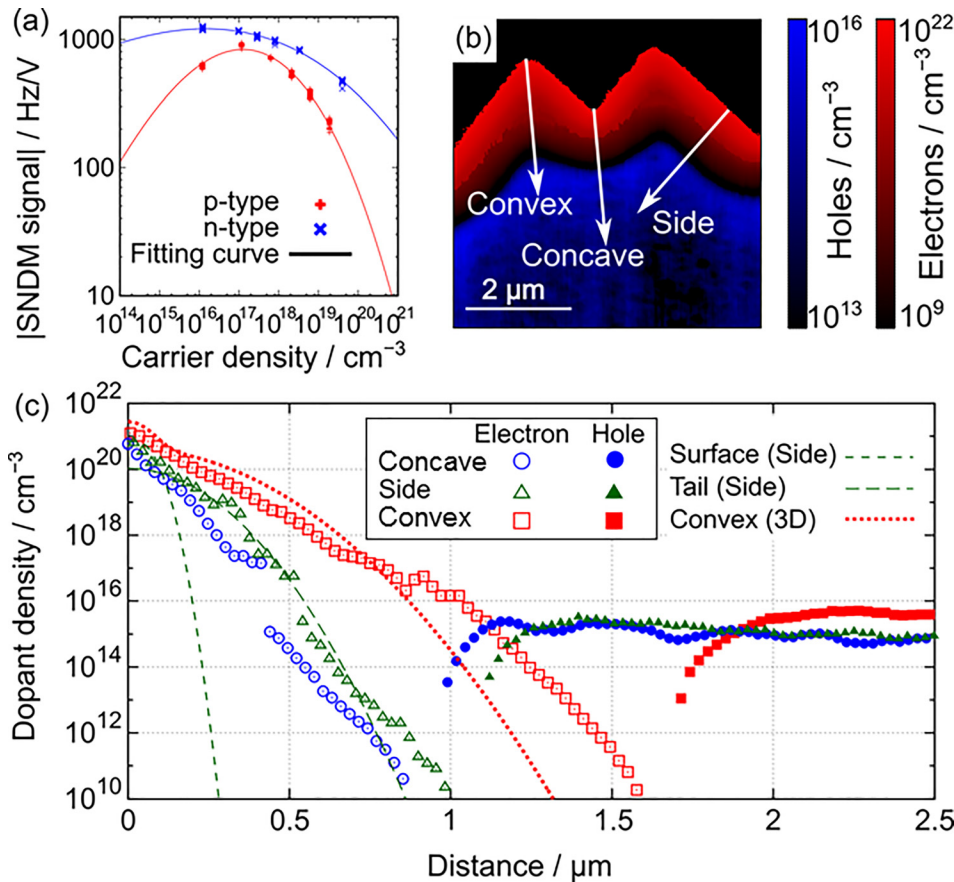


FIG. 4. Carrier density results for cross-section of P-implanted Si solar cell. (a) SNDM results of a Si standard sample and the calibration curve. (b) Two-dimensional carrier density distribution converted using the data in Fig. 1(a). (c) Line profiles through the carrier density distribution in (b). The electron density for the side line is fitted using two Gaussian functions. The dotted red line shows the P density at the convex position obtained from estimation of the 3D P distribution.

that the P distribution in the side region of three dimensional texture structures could be analyzed on the basis of the implanted P distribution in the flat substrate. The error does not stem from the error associated with the measurement.

Figure 4(c) shows that the tail region occupies almost the entire emitter. An effective diffusivity of  $1.3 \times 10^{-13} \text{ cm}^2/\text{s}$  was obtained from the Gaussian function fitting in the tail region. It should be noted that the diffusivity changes during diffusion and is dependent on the dopant density and defect density. The effective diffusivity can approximately describe the diffusion phenomenon. In addition, the positive fixed charges in the SiN layer must cause electrons to accumulate at the textured surface, causing the distribution of electrons to change.

Since each pyramid has four faces, the P distributions in the direction vertical to the faces are expected to be the same. In this case, we can roughly estimate the 3D P distribution in the upper part of the pyramidal base using the superposition of Gaussian functions in Fig. 4(c). (Strictly speaking, the boundary conditions at the edges of the pyramids are different.) Figure 4 shows the 3D carrier distribution using the superposition of P distributions. A line profile at the convex position in Fig. 5 is shown as a dotted line in Fig. 4(c). The line profile obtained from the 3D distribution is in good agreement with that obtained from the SNDM results and has the same order of magnitude.

Moreover, to check the number determined using this method consistent with traditional electric measurements and also to check the acceleration energy dependency on



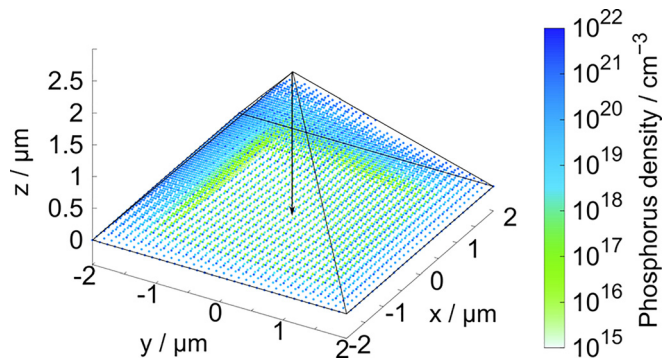


FIG. 5. Estimation of 3D carrier distribution in the upper part of the pyramidal base on the basis of the superposition principle.

effective diffusivity in this method, we prepared the other implanted flat substrate without texture and evaluated P distribution by SIMS in this flat sample. The changed implantation and annealing parameters are only the acceleration energy of 25 keV and the implantation dose of  $4.2 \times 10^{15} \text{ cm}^{-2}$ . The measured P profile in the flat substrate by SIMS is shown in Fig. 6. From this data, we obtained an effective diffusivity of  $1.6 \times 10^{-13} \text{ cm}^2/\text{s}$  in the tail region, which was of the same order as the obtained effective diffusivity at the side region of the actual texture.

However, the authors also note that we should run the same experiments with different implantation doses. The lowest one should be close to the resolution of this technique, to clarify its sensitivity; the highest should be well above the clustering concentration of P in Si to show how the technique behaves when a significant fraction of the implanted ions cluster and are not electrically active. On this issue, we need much more numerous and deeper experiments in the near future.

In summary, the P distribution in a Si solar cell was evaluated using SNDM. The carrier distribution was observed using complementary SNDM and dC/dz-SNDM measurements. The carrier density was quantified using a Si standard sample. The P distributions could be described as two Gaussian functions, and the effective diffusivity was evaluated. In addition, the 3D P distribution was estimated using the superposition principle. The estimated 3D P distribution was in good agreement with the SNDM results. Therefore, it was concluded that SNDM is a useful method for evaluation of the active dopant distribution in Si solar cells. Further

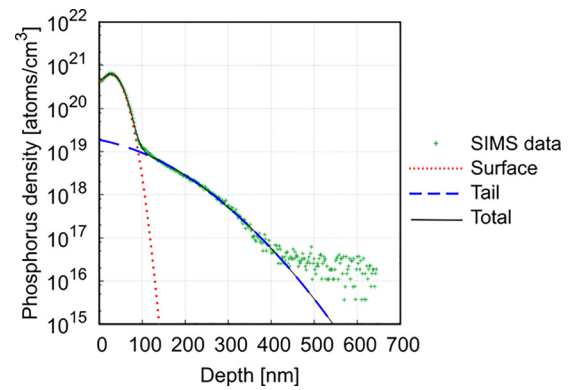


FIG. 6. P density profile in an implanted flat substrate measured by using SIMS.

experimental and theoretical studies are required to improve the device performance. For example, more detailed analysis regarding P diffusion would provide the exact initial P distribution and P diffusivity. In addition, diffusion simulations could lead to the precise estimation of the 3D P distribution. The relationship between the P distribution and implantation conditions can thus be obtained from evaluation of P-implanted Si solar cell fabricated with various implantation or annealing parameters. The conversion efficiency can be estimated from the obtained carrier distribution through device simulations.

This research was supported in part by a Grant-in-Aid for Scientific Research (S) (No. 16H06360) from the Japan Society for Promotion of Science (JSPS).

- <sup>1</sup>H. Hieslmair, I. Latchford, L. Mandrell, M. Chun, and B. Adibi, *Photovoltaics Int.* **18**, 58 (2012).
- <sup>2</sup>T. Michel, J. Le Perche, A. Lanterne, R. Monna, F. Torregrosa, L. Roux, and M. Commandré, *Sol. Energy Mater. Sol. Cells* **133**, 194 (2015).
- <sup>3</sup>H. Sai, Y. Kanamori, K. Arafune, Y. Ohshita, and M. Yamaguchi, *Prog. Photovoltaics: Res. Appl.* **15**, 415 (2007).
- <sup>4</sup>J. R. Matey and J. Blanc, *J. Appl. Phys.* **57**, 1437 (1985).
- <sup>5</sup>K. Tanahashi, M. Morita, Y. Kida, and N. Suzuki, in *31st European Photovoltaic Solar Energy Conference and Exhibition* (2015), pp. 35–38.
- <sup>6</sup>Y. Cho, A. Kiriha, and T. Saeki, *Rev. Sci. Instrum.* **67**, 2297 (1996).
- <sup>7</sup>R. Stephenson, A. Verhulst, P. De Wolf, M. Caymax, and W. Vandervorst, *Appl. Phys. Lett.* **73**, 2597 (1998).
- <sup>8</sup>A. Kikukawa, S. Hosaka, and R. Imura, *Appl. Phys. Lett.* **66**, 3510 (1995).
- <sup>9</sup>D. Mathiot and J. C. Pfister, *J. Appl. Phys.* **55**, 3518 (1984).
- <sup>10</sup>J. F. Gibbons and S. Mylroie, *Appl. Phys. Lett.* **22**, 568 (1973).